Development of highly sensitive nanoscale transition edge sensors for gigahertz astronomy and dark matter search

Journal of Applied Physics

Development of highly sensitive nanoscale transition edge sensors for gigahertz astronomy and dark matter search

Cite as: J. Appl. Phys. **128**, 194502 (2020); https://doi.org/10.1063/5.0021996
Submitted: 16 July 2020 . Accepted: 05 November 2020 . Published Online: 18 November 2020

Federico Paolucci, Vittorio Buccheri, Gaia Germanese, Nadia Ligato, Riccardo Paoletti, Giovanni Signorelli, Massimiliano Bitossi, Paolo Spagnolo, Paolo Falferi, Mauro Rajteri, Claudio Gatti, and Francesco Giazotto

Journal of Applied Physics ARTICLE scitation.org/journal/jap

Development of highly sensitive nanoscale transition edge sensors for gigahertz astronomy and dark matter search

Cite as: J. Appl. Phys. **128**, 194502 (2020); doi: 10.1063/5.0021996
Submitted: 16 July 2020 · Accepted: 5 November 2020 ·
Published Online: 18 November 2020 · Publisher error corrected: 20 November 2020

Federico Paolucci,[1,2,a)] Vittorio Buccheri,[1,2] Gaia Germanese,[1,3] Nadia Ligato,[1] Riccardo Paoletti,[2,4] Giovanni Signorelli,[2] Massimiliano Bitossi,[2] Paolo Spagnolo,[2] Paolo Falferi,[5,6] Mauro Rajteri,[7] Claudio Gatti,[8] and Francesco Giazotto[1,b)]

AFFILIATIONS

[1]NEST, Istituto Nanoscienze-CNR and Scuola Normale Superiore, I-56127 Pisa, Italy
[2]INFN Sezione di Pisa, Largo Bruno Pontecorvo 3, I-56127 Pisa, Italy
[3]Dipartimento di Fisica dell'Università di Pisa, Largo Pontecorvo 3, I-56127 Pisa, Italy
[4]Dipartimento di Scienze Fisiche, della Terra e dell'Ambiente dell'Università di Siena, Strada Laterina 8, I-53100 Siena, Italy
[5]IFN-CNR and Fondazione Bruno Kessler, via alla Cascata 56, I-38123 Povo, Trento, Italy
[6]INFN, TIFPA, via Sommarive 14, I-38123 Povo, Trento, Italy
[7]Istituto Nazionale di Ricerca Metrologica (INRIM), Str. delle Cacce 91, I-10135 Torino, Italy
[8]INFN, Laboratori Nazionali di Frascati, Via Enrico Fermi 54, I-00044 Frascati, Italy

[a)]**Author to whom correspondence should be addressed:** federico.paolucci@nano.cnr.it
[b)]francesco.giazotto@sns.it

ABSTRACT

Terahertz (THz) and sub-terahertz (sub-THz) band detection has a key role in both fundamental interactions physics and technological applications, such as medical imaging, industrial quality control, and homeland security. In particular, transition edge sensors (TESs) and kinetic inductance detectors (KIDs) are the most employed bolometers and calorimeters in the THz and sub-THz band for astrophysics and astroparticles research. Here, we present the electronic, thermal, and spectral characterization of an aluminum/copper bilayer sensing structure that, thanks to its thermal properties and a simple miniaturized design, could be considered a perfect candidate to realize an extremely sensitive class of nanoscale TES (nano-TES) for the giga–terahertz band. Indeed, thanks to the reduced dimensionality of the active region and the efficient Andreev mirror heat confinement, our devices are predicted to reach state-of-the-art TES performance. In particular, as a bolometer the nano-TES is expected to have a noise equivalent power of 5×10^{-20} W/$\sqrt{\text{Hz}}$ and a relaxation time of ∼10 ns for the sub-THz band, typical of cosmic microwave background studies. When operated as a single-photon sensor, the devices are expected to show a remarkable frequency resolution of 100 GHz, pointing toward the necessary energy sensitivity requested in laboratory axion search experiments. Finally, different multiplexing schemes are proposed and sized for imaging applications.

I. INTRODUCTION

In the last decade, astronomy and astrophysics have broadened their interest toward low energy phenomena, such as cosmic microwave background (CMB),[1] atomic vibrations in galaxy clusters,[2] and new particles in dark matter.[3] To obtain physical insight of these phenomena, the detection of faint signals in the micro- (terahertz) and sub-millimeter (gigahertz, GHz) spectral range plays a fundamental role. To this end, the key ingredient is the development of new ultrasensitive bolometers and single-photon detectors, i.e., calorimeters. On the one hand, the temperature and polarization maps of the CMB fluctuations[4,5] and the detection of polarized radiation due to the hydrogen atom emission in the galaxy clusters[6] are the

main astronomy applications for gigahertz (GHz) and terahertz (THz) bolometers. On the other hand, low frequency calorimeters could play a fundamental role in axions search,[7] one of the principal candidates for the dark matter. Axions are very weakly interacting particles with small mass (∼1 meV), thus impossible to be revealed by means of colliders. Therefore, light-shining-through-wall (LSW) experiments have been proposed to generate axion-like particles (ALPs) in the laboratory,[8] differently from experiments focused on space surveys, such as CAST[9] and IAXO.[10]

Nowadays, the most employed detectors in the THz energy band are the superconducting sensors, such as transition edge sensors (TESs)[11–13] and kinetic inductance detectors (KIDs),[14] for their high sensitivity, robustness, and mature technology. The state-of-the-art of these detectors in bolometric operation shows a noise equivalent power (NEP) of $\sim 10^{-19}\ \mathrm{W}/\sqrt{\mathrm{Hz}}$ for TESs[15] with large active area ($\sim 100\,\mu\mathrm{m}^2$) and $\sim 10^{-18}\ \mathrm{W}/\sqrt{\mathrm{Hz}}$ for KIDs.[16] More sensitive and efficient superconducting detectors have been proposed and realized by taking advantage of device miniaturization[17] and the Josephson effect. For instance, detectors based on superconductor/normal metal/superconductor (SNS) junctions showed a *NEP* of the order of $10^{-20}\ \mathrm{W}/\sqrt{\mathrm{Hz}}$,[18] cold electron bolometers showed a *NEP* of $\sim 3 \times 10^{-18}\ \mathrm{W}/\sqrt{\mathrm{Hz}}$,[19] devices based on the temperature-to-phase conversion (TPC) are expected to provide a *NEP* of $\sim 10^{-23}\ \mathrm{W}/\sqrt{\mathrm{Hz}}$,[20] while a fully superconducting tunable Josephson escape sensor (JES) showed a record intrinsic *NEP* as low as $10^{-25}\ \mathrm{W}/\sqrt{\mathrm{Hz}}$.[21]

To push the TES technology toward lower values of *NEP* with the possibility to detect single photons in the GHz band,[22] a strong reduction of the thermal exchange mechanisms of the active region, i.e., the portion of the device transitioning to the normal state when radiation is absorbed, is necessary.[23] To this end, we envision a nanoscale TES (nano-TES) exploiting a simple and sturdy miniaturized design together with the Andreev mirrors (AMs) effect[24] to thermally isolate the sensor active region. Here, we present and experimentally characterize the active region of the nano-TES structures by an electrical and a thermal point of view. For simplicity, we will adopt the notation nano-TES to indicate the structures analyzed in this paper. Indeed, operating in the bolometer configuration our nano-TESs would reach a total noise equivalent power (NEP_{tot}) of $\sim 10^{-20}\ \mathrm{W}/\sqrt{\mathrm{Hz}}$, while as calorimeters they are expected to reach a resolving power ($\delta\nu/\nu$) of 10 in the sub-THz band. Their measured thermal and electrical performances are several orders of magnitude better than devices with identical dimensions but without the Andreev mirrors heat constrictions. Finally, we propose and size two possible multiplexing circuits in frequency domain (FDM) and microwave resonator (MR) as a readout for a nano-TES array enabling the realization of multi-pixel cameras. In addition to gigahertz astronomy and particle physics, the nano-TES could find applications for medical imaging,[25] industrial quality controls,[26] and security.[27]

This paper is organized as follows. Section II reports the simple fabrication of the nano-TES and of a secondary device used to extract all the parameters of the active region. Section III describes the electrical properties of the nano-TES. The spectral and thermal characterization of the active region is resumed in Secs. IV and V, respectively. The expected nano-TES performance as a bolometer and a calorimeter deduced from the experimental data is reported in Sec. VI together with the comparison of a TES of identical materials and dimensions but not equipped with AM. Finally, Sec. VII covers possible multiplexing readout circuits to design multi-pixel cameras.

II. DEVICES FABRICATION

The experiments discussed in this paper are performed thanks to two different device architectures: the nano-TES and a secondary device (SD). Measurements on the nano-TES provided the active region resistance vs temperature characteristics $R_A(T)$, the active region critical I_c and retrapping I_r current, and the critical temperature T_c. Instead, the active region spectral and thermal properties have been obtained by the experiments performed on the SD.

The false-color scanning electron microscope (SEM) pictures of a typical nano-TES and SD are shown in Figs. 1(a) and 1(b), respectively. The nano-TES, highlighted by the dashed white box in Fig. 1(a), consists in a 1.5 μm-long, 100 nm-wide, and 25 nm-thick Al/Cu bilayer nanowire-like active region (red), which is sandwiched between the Al electrodes (blue). Since the superconducting gap of the Al layer is higher than that of the Al/Cu bilayer (due to the inverse proximity effect[28]), the electrodes act as AM for the active region, leading to the advantages discussed in Sec. V. The same nano-TES structure is visible in the SD [see Fig. 1(b)] with the addition of two oxidized Al probes (yellow) lying under the active region and forming two tunnel Josephson junctions (JJs).[29] These two Al probes allow one to characterize both the energy gap and the thermal properties of the active region.

Both the nano-TES and the SD were realized during the same fabrication process, ensuring the homogeneity of their properties. They were fabricated by electron-beam lithography (EBL) and three-angles shadow mask evaporation of metals onto a silicon wafer covered with 300 nm of thermally grown SiO_2. The evaporation was performed in an ultra-high vacuum electron-beam evaporator with a base pressure of about 10^{-11} Torr. By referring to the color code of Figs. 1(a) and 1(b), the first Al layer (yellow) with a thickness of 13 nm was evaporated at an angle of $-40°$ and then oxidized by exposition to 200 mTorr of O_2 for 5 min to obtain the tunnel probes in the SD. In a second step, the Al/Cu bilayer (red) was evaporated at an angle of 0° to form the active region with partial thicknesses $h_{\mathrm{Al}} = 10.5$ nm and $h_{\mathrm{Cu}} = 15$ nm for the aluminum and copper layers, respectively. Finally, a second Al layer (blue) of thickness 40 nm was evaporated at an angle of $+40°$ to obtain the AM electrodes.

The notations *A*, *S*, *P*, and *I* will be used to indicate the Al/Cu active region, the Al electrodes, the Al probes, and the probes insulating barrier, respectively. The nano-TES measurements have been performed on two different devices, n-T1 and n-T2. All the following experiments have been performed in a ^{3}He-^{4}He dilution refrigerator with bath temperature T_{bath} ranging from 20 mK to 250 mK.

III. NANO-TES ELECTRICAL PROPERTIES

The four-terminal voltage–current *VI* characteristics of n-T1 are shown in Fig. 1(c) at $T_{bath} = 20$ mK for a positive (gray line) and a negative (yellow line) current slope. The electrical measurement setup is schematized in the inset. Here, the normal $\mathcal{N}$ and the superconducting $\mathcal{S}$ state are recognizable by the linearly growing and the flat behavior of the *VI* traces, respectively. The

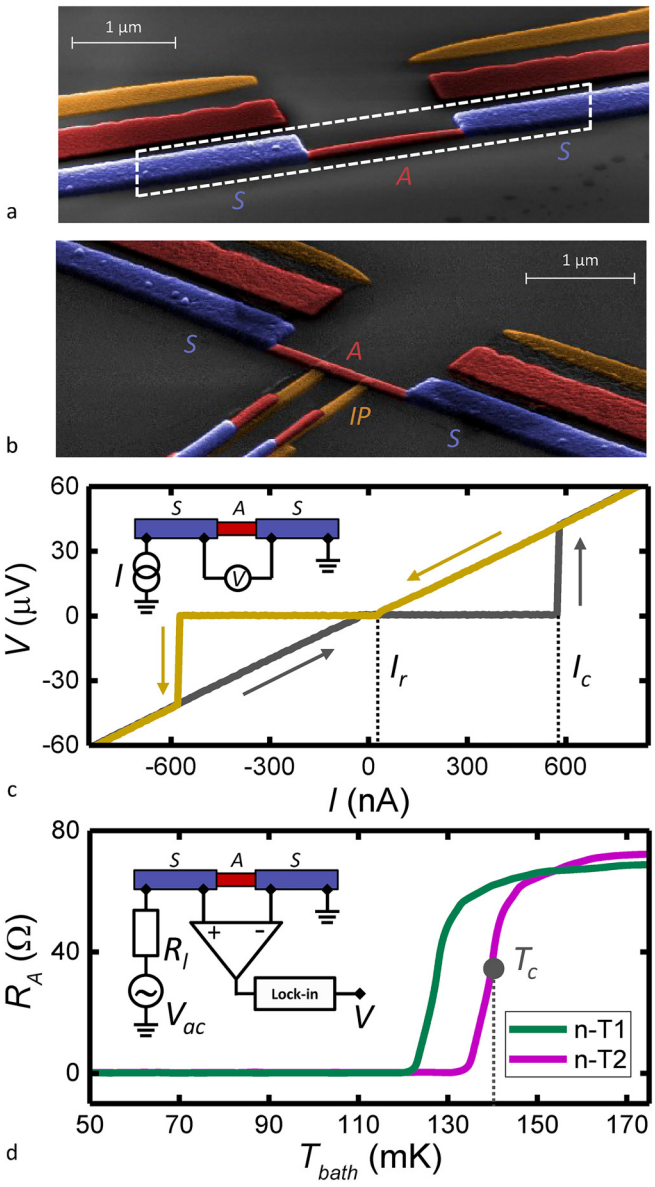

FIG. 1. False-color SEM pictures of the nano-TES (a) and SD (b). The three different layers are the active region Al/Cu bilayer *A* (red), the Al electrodes *S* (blue), and the Al-oxidized tunnel probes *IP* (yellow). The detector structure is pointed out by the dashed white box in the nano-TES SEM. (c) Four-terminal *VI* measurement of sample n-T1 for a positive (gray line) and a negative (yellow line) current slope at $T_{bath} = 20$ mK. The black dotted lines highlighted the critical current $I_c \sim 600$ nA and the retrapping $I_r \sim 27$ nA of *A*, where the $\mathcal{S} \rightarrow \mathcal{N}$ and the $\mathcal{N} \rightarrow \mathcal{S}$ transitions occur, respectively. *Inset*: Experimental setup for the *VI* measurement. (d) Temperature dependence of the nano-TES active region resistance, R_A, for n-T1 (green line) and n-T2 (purple line). By following a positive T_{bath} slope, R_A goes from zero to the normal state resistance value. The critical temperature T_c (gray point for n-T2) is the temperature corresponding to the half of the normal resistance of the samples. *Inset*: Experimental setup for the R_A vs T_{bath} measurements.

$\mathcal{S} \rightarrow \mathcal{N}$ transition occurs at the critical current $I_c \sim 600$ nA, whereas the $\mathcal{N} \rightarrow \mathcal{S}$ occurs at the retrapping current $I_r \sim 27$ nA.[30] The normal-state resistance R_A is obtained by the slope of the *VI* and gets the value $R_{A,n-T1} = 70\ \Omega$, while it is obviously zero in the $\mathcal{S}$. This change of R_A has a key role in the operation mechanism of a TES detector[12] (see Sec. VII for further details).

The temperature dependence of R_A is shown in Fig. 1(d) for n-T1 (green line) and n-T2 (purple line). The inset shows the experimental setup. The AC current bias is produced by applying a voltage V_{ac} at 13.33 Hz to a load resistance $R_l = 100$ kΩ ($R_l \gg R_A$) in order to obtain $I_{ac} = 15$ nA independent of R_A. The voltage drop V across the nano-TES is measured as a function of T_{bath} via a voltage preamplifier connected to a lock-in amplifier. By increasing T_{bath}, the resistance changes from zero to its normal-state value, by following an edge transition behavior. The nano-TES critical temperature T_c is defined as the temperature corresponding to half of the normal-state resistance [gray point for n-T2 in Fig. 1(d)]. Thus, we have $T_{c1} = 128$ mK and $T_{c2} = 139$ for n-T1 and n-T2, respectively.

IV. SPECTRAL CHARACTERIZATION OF THE ACTIVE REGION

For $T < 0.4T_c$, the energy gap of a superconductor [$\Delta(T)$] is temperature independent and equals its zero-temperature value Δ_0.[28] For higher values of temperature, $\Delta(T)$ decreases monotonically and finally disappears at T_c. Typically, aluminum thin films show a T_c higher than the bulk Al value (~1.2 K).[31] Therefore, the superconducting gaps of *S* and *P*, $\Delta_S(T)$ and $\Delta_P(T)$, are temperature independent up to at least 500 mK, thus preserving their zero-temperature values ($\Delta_{0,S}$ and $\Delta_{0,P}$). By contrast, due to the inverse proximity effect,[28] superconductivity in *A* is strongly suppressed. In fact, our resistance vs temperature experiments showed a value $T_{c,A} \simeq 140 \ll 500$ mK [see Fig. 1(d)], thus enabling the possibility to independently determine both $\Delta_{0,A}$ and $\Delta_{0,P}$.

To this end, the *IV* characteristics of a *SAIP* JJ were measured at base temperature and just above $T_{c,A}$, as reported in Fig. 2(a) with the gray and the green lines, respectively. The experimental setup of the measurements is schematically shown in the inset of the panel. At base temperature, the JJ switches to the $\mathcal{N}$-state when the voltage bias reaches $V_{SAIP} = \pm(\Delta_{0,A} + \Delta_{0,P})/e$,[29] where e is the elementary charge. Instead, at $T_{bath} = 250$ mK, the transition occurs at $V_{SAIP} = \pm\Delta_{0,P}/e$ since *A* is in the $\mathcal{N}$-state. The tunnel resistance of the JJ is given by the slope of the *IV* characteristic in the linear region, as highlighted by the black dotted line and gets value $R_I \simeq 12$ kΩ.

In order to provide a precise evaluation of the energy gaps, the *IV* characteristics are zoomed around the switching points acquired for positive voltage bias, as shown in Fig. 2(b). The measurement at $T_{bath} = 250$ mK (green line) indicates a value of the zero-temperature superconducting gap of the aluminum probes $\Delta_{0,P} \simeq 200\,\mu$eV, corresponding to a critical temperature $T_{c,P} = \Delta_{0,P}/(1.764k_B) \simeq 1.3$ K. Note that $\Delta_P \sim \Delta_S$ since electrodes and probes thickness are similar,[34] thus $T_{c,S} \sim 1.3$ K as well. Instead, the difference between the results obtained at 20 mK and 250 mK leads to $\Delta_{0,A} \simeq 23\,\mu$eV corresponding to a critical temperature $T_{c,A} \simeq 150$ mK, in good agreement with the data reported in Fig. 1(d).

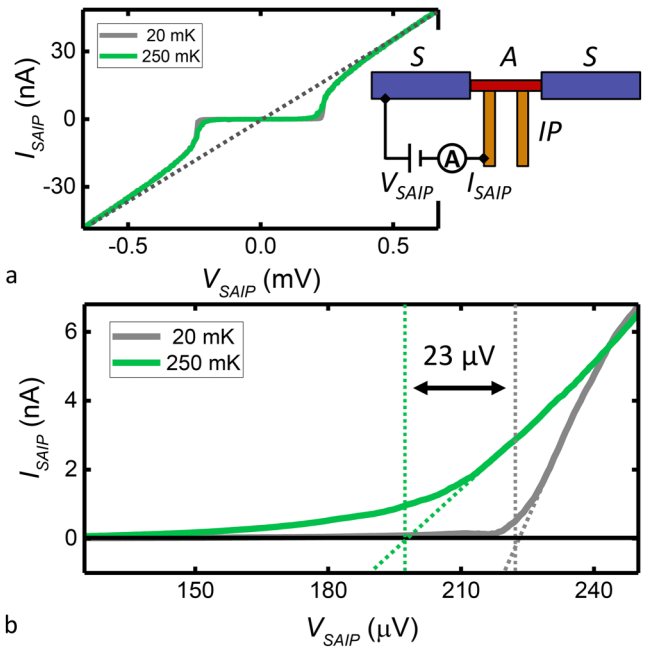

FIG. 2. (a) The *IV* characteristic of the *SAIP* junction at $T_{bath} = 20$ mK (gray line) and $T_{bath} = 250$ mK (green line). The slope of the linear region (dotted line) represents the $\mathcal{N}$-state tunnel resistance of the JJ, $R_J \simeq 12\,\text{k}\Omega$. *Inset*: Schematic representation of SD with the experimental setup used for the spectral characterization. (b) The *IV* characteristics of the *SAIP* junction zoomed on the positive switching point for two bath temperatures: the high temperature switching point corresponds to $\Delta_{0,P} \simeq 200\,\mu$eV, while the difference between the two onset points is $\Delta_{0,A} \simeq 23\,\mu$eV.

Importantly, the superconducting gap of A is constant along the out-of-plane axis (i.e., the sample thickness), because the bilayer is within the Cooper limit.[32,33] In fact, the aluminum thin film follows $h_{\text{Al}} = 10.5\,\text{nm} \ll \xi_{0,\text{Al}} = \sqrt{\hbar D_{\text{Al}}/\Delta_{0,\text{Al}}} \simeq 80\,\text{nm}$ (where $D_{\text{Al}} = 2.25 \times 10^{-3}\,\text{m}^2\,\text{s}^{-1}$ is the diffusion constant of Al and $\Delta_{0,\text{Al}} \simeq 200\,\mu$eV is the superconducting energy gap), while the copper layer respects $h_{\text{Cu}} = 15\,\text{nm} \ll \xi_{0,\text{Cu}} = \sqrt{\hbar D_{\text{Cu}}/(2\pi k_B T)} \simeq 255\,\text{nm}$ (where $D_{\text{Cu}} = 8 \times 10^{-3}\,\text{m}^2\text{s}^{-1}$ is the copper diffusion constant and the temperature is chosen $T = 150$ mK thus higher than the nano-TES operation value). Furthermore, the active region is much thinner than its superconducting coherence length, that is, $h_A = h_{\text{Al}} + h_{\text{Cu}} = 25.5\,\text{nm} \ll \xi_A = \sqrt{l\hbar/[(h_{\text{Al}}N_{\text{Al}} + h_{\text{Cu}}N_{\text{Cu}})R_A e^2 \Delta_{0,A}]} \simeq 220\,\text{nm}$, where e is the electron charge, while $N_{\text{Al}} = 2.15 \times 10^{47}\ \text{J}^{-1}\text{m}^{-3}$ and $N_{\text{Cu}} = 1.56 \times 10^{47}\ \text{J}^{-1}\text{m}^{-3}$ are the density of states (*DOSs*) at the Fermi level of aluminum and copper, respectively.

V. THERMAL CHARACTERIZATION OF THE ACTIVE REGION

Energy exchange has a key role in determining the nano-TES performance, such as sensitivity and response time, since the increase of the A electronic temperature T_A due to the incident radiation strongly depends on the capability of maximizing the thermal confinement. The scope of this section is to study the most prominent heat exchange mechanisms in the active region of the nano-TES for typical operating conditions.

Metallic elements in mesoscopic devices at sub-kelvin temperatures show weak coupling between the electron and the phonon thermal subsystems,[29] which can lead to $T_e \neq T_{ph}$, where T_e and T_{ph} are the electron and phonon temperature, respectively. Due to the thickness of the films lower than the phonon wavelength and vanishing Kapitza resistance, the device phonons are thermally anchored to the substrate ($T_{ph} = T_{sub}$)[35] so that the temperature of both systems can be considered a parameter set via the refrigerator temperature T_{bath}. The geometry of our device also guarantees electronic temperature of the superconducting electrodes T_S and the tunnel probes T_P equal to the phonon temperature, that is, $T_S = T_P = T_{bath}$. By contrast, the A electronic temperature T_A is the fundamental thermal variable in the nano-TES operation mechanism. In general, the value of T_A results from the balance between the main thermal exchange channels of A. In our case,

$$P_{in} = P_{e-ph} + P_{AIP} + P_{loss}, \tag{1}$$

where P_{in} is the power injected, P_{e-ph} is the electron–phonon relaxation, P_{loss} represents the heat losses through S, and P_{AIP} is the energy diffusion by an *IP* probe. Note that the electron–photon interaction contribution has not been considered in the model since it is negligibly small in comparison to the other thermal channels.[36]

The use of S with energy gap much larger than A can ensure negligible heat out-diffusion from A to S. Indeed, the normalized *DOS* of a superconductor reads[29]

$$DOS(E, T) = \frac{|E|}{\sqrt{E^2 - \Delta^2(T)}}\Theta(E^2 - \Delta^2(T)). \tag{2}$$

Thus, the zero-temperature energy-dependent *DOSs* of S and A are calculated by inserting the measured values of $\Delta_{0,S}$ and $\Delta_{0,A}$. The resulting functions are shown in Fig. 3(a) with the blue and the red lines, respectively. The thermally excited quasi-particles in A do not find available states toward S; thus, the resistance for heat diffusion exponentially rises by decreasing the bath temperature.[24] In particular, at $k_B T_A \ll \Delta_S$, the superconducting leads act as AM, namely, as perfect barriers for energy diffusion ($P_{loss} = 0$). In addition, the big difference between the two superconducting gaps ensures that the nano-TES superconducting to dissipative transition affects only A, leading to a better control in the resistance change and a small overheating of the detector.

The experimental setup employed to perform the thermal study of A is schematically shown in Fig. 3(b): the left *SAIP* junction was current-biased (at I_{bias}) to operate as a thermometer, whereas the right JJ was voltage-biased (at V_{heater}) to work as a heater.[29] The thermometer has been calibrated by varying T_{bath} and measuring V_{Tmeter} at $I_{bias} = 10\,\text{pA}$ and $V_{heater} = 0\,\text{V}$, as reported in Fig. 3(c). The bath temperature ranges from ~150 mK to ~350 mK, so $\Delta_A = 0$, i.e., A is in the normal state, whereas $\Delta_S \simeq 200\,\mu$eV. In this normal metal (A)/insulator/superconductor

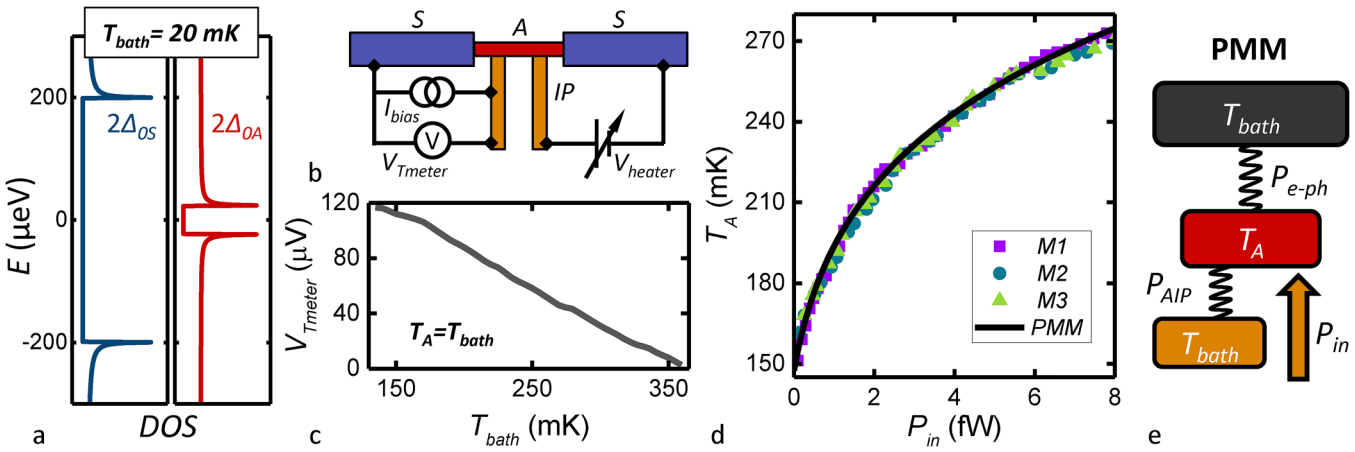

FIG. 3. (a) BCS *DOS*s of *S* (blue) and *A* (red) at $T_{bath} = 20$ mK with the gaps obtained experimentally, $\Delta_A = 23\,\mu$eV and $\Delta_S = 200\,\mu$eV. (b) Schematic representation of the experimental setup used for the thermal characterization: the left and the right *SAIP* JJs are used as electron thermometer and heater, respectively. (c) Thermometer calibration curve that links the voltage output V_{Tmeter} to the *A* electronic temperature T_A. (d) Electronic temperature of *A* as a function of the input power for three different data sets *Mi*, with $i = 1, 2, 3$ (colored symbols) at $T_{bath} = 150$ mK. The fitting curve (black line) is obtained by solving Eq. (3) of the PMM. (e) PMM thermal model of *A*: the input power from the heater P_{in} relaxes through the outward components: P_{e-ph}, due to the electron–phonon interaction, and P_{AIP}, due to the losses through the thermometer tunnel junction.

(*P*) JJ, the *IV* characteristics depend only on the electronic temperature of the normal metal.[29] Therefore, the values of V_{Tmeter} directly reflect T_A.[37]

The heater has been calibrated by acquiring the current-to-voltage characteristic of the tunnel junction at the different values of T_{bath}. In particular, the injected power is given by $P_{in} = 0.5 V_{heater} I_{heater}$, where the factor 0.5 stems from the fact that the heat is equally dissipated on the two sides of the junction. In this experimental configuration, the heat is generated at one side of the active region, while the thermometer is placed in the vicinity of the opposite end [see Figs. 1(b) and 3(b)]. The electrons is *A* thermalize through electron–electron interaction and electron–phonon scattering, while the heat losses through the thermometer tunnel junction is negligible compared to the other contributions (see Subsection V A). As a consequence, the electronic temperature in the active region varies for distances of the order of the electron–phonon coherence length $l_{e-ph} = \sqrt{D_{Ave}\tau_{e-ph}} = 180\,\mu$m,[29] where $D_{Ave} = (t_{Al}D_{Al} + t_{Cu}D_{Cu})/(t_{Al} + t_{Cu}) \simeq 5.6 \times 10^{-3}\,\mathrm{m^2/s}$ is the diffusion constant of the active region and $\tau_{e-ph} = 6\,\mu$s is the electron–phonon scattering time (see Sec. VI A for details). Since the length of the active region is $L = 1.5\,\mu\mathrm{m} \ll l_{e-ph}$, we can assume that the electronic temperature in the active region is homogeneous during our experiments.

A. Perfect Andreev mirrors

Figure 3(d) shows T_A as a function of the input power acquired at $T_{bath} = 150$ mK in three different sets of measurements. The electronic temperature monotonically increases from 150 mK to ∼270 mK by increasing P_{in} to ∼8 fW. Within the experimental parameters, the inequality $k_B T_A \ll \Delta_{0,S}$ is always satisfied. Therefore, the perfect mirror model (PMM) can describe the data: the heat exchange between *A* and *S*s is fully suppressed ($P_{loss} = 0$), i.e., *A* is thermally isolated from *S*. Thus, the injected power P_{in} relaxes only via electron–phonon interaction P_{e-ph} and out-diffuses through the thermometer *IP* P_{AIP}. The resulting quasi-equilibrium equation describing the PMM reads

$$P_{in} = P_{e-ph} + P_{AIP}, \tag{3}$$

as schematically represented in Fig. 3(e).

Since *A* is in the $\mathcal{N}$-state, the power exchanged via electron–phonon interaction can be written as[29]

$$P_{e-ph} = \Sigma_A \mathcal{V}_A \left(T_A^5 - T_{bath}^5\right), \tag{4}$$

where Σ_A is the electron–phonon thermal relaxation constant and $\mathcal{V}_A$ is the volume of *A*. The power that flows through the thermometer JJ takes the form[29]

$$P_{AIP} = \frac{1}{e^2 R_{Tmeter}} \int_{-\infty}^{+\infty} \mathrm{d}E\, E\, DOS_P(E, T_{bath}) \times [f_0(E_A, T_A) - f_0(E, T_{bath})], \tag{5}$$

where $DOS_P(E, T_{bath})$ is the *DOS* of the superconducting probe, $E_A = E - eV_{Tmeter}$ is the energy of the active region, and $f_0(E, T_{A,bath}) = [1 + \exp(E/k_B T_{A,bath})]^{-1}$ is the Fermi–Dirac distribution of *A* and *P*, respectively.

By solving Eq. (3), we fit the experimental electronic temperature of the *A* as a function of P_{in}, as shown by the black line in Fig. 3(d). Since all the other device parameters are known ($\mathcal{V}_A = 38 \times 10^{-22}\,\mathrm{m^3}$, $R_{Tmeter} = 11.6\,\mathrm{k\Omega}$ and $T_{bath} = 150$ mK), we extracted the value of the electron–phonon coupling constant of

the Al/Cu bilayer $\Sigma_A \simeq 1.3 \times 10^9$ W/m^3 K^5. We notice that the PMM provides a remarkable fit of the experimental data, thus describing correctly the system. The contribution of the electron–phonon relaxation is about one order of magnitude larger than the thermal losses through the thermometer tunnel junction. Therefore, the presence of the thermometer tunnel barrier has a negligible impact on the thermal experiment. Furthermore, the resulting electron–phonon relaxation constant is in good agreement with the average of $\Sigma_{Cu} = 2.0 \times 10^9$ W/m^3 K^5 and $\Sigma_{Al} = 0.2 \times 10^9$ W/m^3 K^5,[29] weighted with the volumes of the copper and the aluminum layer forming the active region: $\Sigma_{A,theo} = (\Sigma_{Cu}\mathcal{V}_{Cu} + \Sigma_{Al}\mathcal{V}_{Al})/\mathcal{V}_A = 1.38 \times 10^9$ W/m^3 K^5, with $\mathcal{V}_{Al} \simeq 1.58 \times 10^{-21}$ m^{-3} and $\mathcal{V}_{Cu} \simeq 2.25 \times 10^{-21}$ m^{-3}.

B. Low-efficiency Andreev mirrors

In order to test the AM efficiency and the limits of the PMM, we investigated the dependence of T_A on larger values of P_{in}. The PMM fails for $P_{in} \geq 9$ fW [the red shaded area in Fig. 4(a)], where the power loss through the S-electrodes is no longer negligible ($P_{loss} \neq 0$) and the resulting increase of T_A is reduced.

The energy losses through the superconducting electrodes can be evaluated by calculating the difference between the measured P_{in} necessary to produce a specific T_A and its value estimated from the PMM. The dependence of P_{loss} on T_A is shown in Fig. 4(b) for different values of T_{bath}. For all the curves, the energy loss through the Andreev mirrors is negligible until reaching a threshold temperature T_x. Notably, for all measurements, we obtain $T_x \simeq 280$ mK [see the inset of Fig. 4(b)], independently from the value of T_{bath} and thus T_S. Furthermore, the energy filtering of the superconducting electrodes starts to fail for $T_x/T_{c,S} \sim 0.22$, which is in good agreement with the theoretical prediction of Andreev $\sim 0.3\,T_c$.[24] Finally, the staircase behavior of P_{loss} present at $T_A > 280$ mK [see Fig. 4(b)] could be due to the superconducting proximity effect at the A/S interface. However, a complete explanation of such behavior would require further measurements and analysis.

The T_A vs P_{in} characteristics change dramatically in a mirrorless device. Indeed, in a TES based on the same structure and dimensions but without AMs, the active region extends to the entire device, i.e., it is composed by a single superconductor. Figure 4(c) shows the difference between our nano-TES (solid lines) and a TES without the Andreev mirrors (dashed lines) calculated for the same values of bath temperature of our experiments. As expected, at a given value of P_{in} the temperature of the active region rises more in the presence of energy filtering than in a composite device, since the main channel for thermalization, the electron–phonon coupling, linearly depends on the volume [see Eq. (4)]. As a consequence, the presence of Andreev mirrors promises enhanced sensitivity of the nano-TES.

VI. NANO-TES PERFORMANCE

This section is devoted to the prediction of the performance of our device when operated as a radiation sensor. Our study will focus on both the bolometric operation, i.e., in continuous incident radiation, and the calorimetric operation, i.e., in single-photon detection. Moreover, we propose a comparison between this device and an identical one without AM.

The typical readout circuit for a TES is schematized in Fig. 5. On the one hand, the decrease of the current I_{TES} flowing through the inductance L due to photon absorption can be measured by means of an inductively coupled superconducting quantum interference device (SQUID) amplifier. On the other hand, the shunt

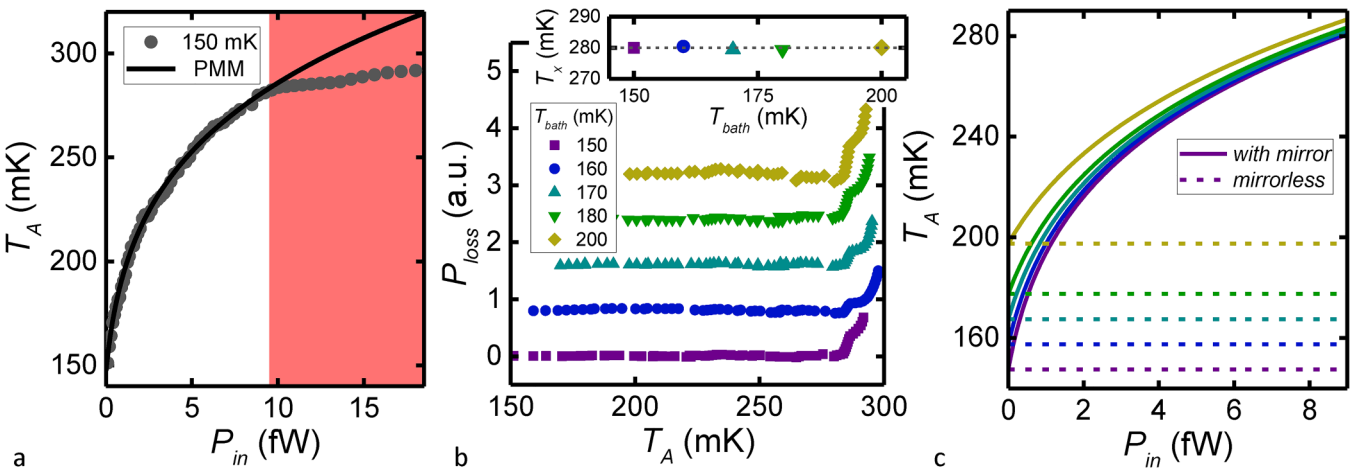

FIG. 4. (a) Electronic temperature of the active region vs input power measured (gray points) and calculated with the PMM (black line) at $T_{bath} = 150$ mK. The red shaded area highlights the values of T_A, where the PMM fails to describe the experimental data. (b) Power diffusion toward the superconducting leads P_{loss} calculated as the difference between the experimental data and PMM theoretical curve at each T_A for different values of T_{bath}. The curves have been vertically shifted for clarity. *Inset*: Threshold temperature T_x as a function of T_{bath}. $P_{loss} \neq 0$ for $T_A \geq 280$ mK independently from T_{bath}. (c) Calculated T_A vs P_{in} characteristics calculated in the presence (solid lines) and absence (dashed lines) of Andreev mirrors for different values of T_{bath}. The color code for T_{bath} follows panel (c). The presence of Andreev mirrors is expected to strongly improve the power sensitivity of the nano-TES.

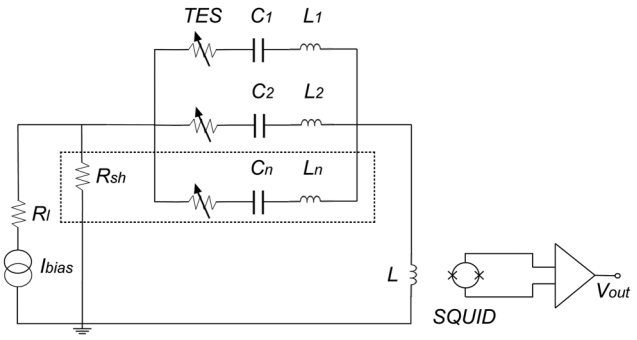

FIG. 5. Schematic of the readout circuit of a single nano-TES. The dashed line highlights the circuit providing the negative electro-thermal feedback NETF, where the nano-TES is biased by the current I_{TES} and operates in parallel to the shunt resistor R_{sh}. The I_{TES} variations are measured with a SQUID amplifier coupled to the circuit by an inductance L.

resistor R_{sh} implements the negative electro-thermal feedback mechanism (NETF), which guarantees the constant voltage bias of the nano-TES and faster heat removal after radiation absorption.[38] To this end, the shunt resistor needs to satisfy the relation $R_{sh} \ll R_A$.[39] In the following, we will use a value $R_{sh} = 10\,\mathrm{m\Omega}$ typical for SQUID amplifier-based readout.

A. Bolometer

Starting from the structure and the measured parameters, we evaluate the performance of our nano-TESs in terms of response time τ and *NEP*. The parameters that we will deduce in this section are reported in Table I.

The thermal response time τ defines the dissipation rate of the overheating arising from radiation absorption in A. The value of τ is related to the quasi-particle thermalization with the phonons residing at T_{bath}. Namely, it depends on the electron heat capacity $C_{e,A}$ and the thermal conductance $G_{th,A}$ of A through[12]

$$\tau = \frac{C_{e,A}}{G_{th,A}}. \tag{6}$$

The A electron heat capacitance reads

$$C_{e,A} = \Upsilon_A \mathcal{V}_A T_{c,A}, \tag{7}$$

with Υ_A being the Sommerfeld coefficient of A. Since A is formed by an Al/Cu bilayer, we have to substitute $\Upsilon_A \mathcal{V}_A = \Upsilon_{Cu} \mathcal{V}_{Cu} + \Upsilon_{Al} \mathcal{V}_{Al}$ (with $\Upsilon_{Cu} = 70.5\,\mathrm{J\,K^{-2}\,m^{-3}}$ and $\Upsilon_{Cu} = 91\,\mathrm{J\,K^{-2}\,m^{-3}}$) in Eq. (7).

The A total thermal conductance $G_{th,A}$ is the derivative of the heat losses of A with respect to its electronic temperature.[12,29] Considering the nano-TES operation at $T_{c,A} \ll T_{c,S}$, we can consider $P_{loss} = 0$; thus, electron–phonon relaxation is the only relevant thermal exchange mechanism. Therefore, the total thermal conductance reads

$$G_{th,A} = \frac{dP_{e-ph}}{dT_A} = 5\Sigma_A \mathcal{V}_A T_A^4. \tag{8}$$

In our nano-TESs, the electron heat capacitance is $C_{e,A_1} = 4 \times 10^{-20}$ J/K for n-T1 ($C_{e,A_2} = 4.2 \times 10^{-20}$ J/K for n-T2), while the thermal conductance is as low as $G_{th,A_1} = 6.7 \times 10^{-15}$ W/K ($G_{th,A_2} = 9.3 \times 10^{-15}$ W/K). As a consequence, the active region relaxation time is limited by $G_{th,A}$ to a few microseconds for both devices ($\tau_1 \simeq 6\,\mu$s and $\tau_2 \simeq 5\,\mu$s).

The negative electro-thermal feedback (see Fig. 5) affects the thermal response of the nano-TES. In particular, the sharpness of the superconducting to normal-state phase transition defines the effective recovery time through $\tau_{eff} = \frac{\tau}{1+\alpha/n}$, where typically $n = 5$ for a clean metal and $\alpha = \frac{d\log(R)}{d\log(T)}$ is the electro-thermal parameter that takes into account the sharpness of the transition from the superconducting to the normal state. As reported in Table I, τ_{eff} is one or two orders of magnitude smaller than the thermal response time ($\tau_{eff} \ll \tau$). Namely, the effective response time is $\tau_{eff,1} = 0.01\,\mu$s and $\tau_{eff,2} = 0.2\,\mu$s for n-T1 and n-T2, respectively.

The *NEP* is the most important figure of merit for a bolometer since it determines the minimum power that can be detected above the noise level. Taking into account the equivalent circuit, highlighted by the dashed line in Fig. 5, the total *NEP* of the nano-TES is given by three uncorrelated sources[40,41]

$$NEP_{tot} \simeq \sqrt{NEP_{TFN}^2 + NEP_{Jo}^2 + NEP_{sh}^2}, \tag{9}$$

where NEP_{TFN} is associated with the thermal fluctuations, NEP_{Jo} is due to the Johnson noise in the nano-TES, and NEP_{sh} is related to the shunt resistor. Other external noise contributions, such as the noise of the readout electronics and the photon background noise, are not taken into account because they cannot be directly attributed to the device.

TABLE I. Principal figures of merit. The time constant τ, the pulse recovery time τ_{eff}, the Noise Equivalent Power due to the thermal fluctuation noise NEP_{TFN} and the total noise NEP_{tot}, the Frequency Resolution $\delta\nu$, and the Resolving Power $\nu/\delta\nu$ (at 100–300–1000 GHz) are reported for two fabricated nano-TESs (n-T1 and n-T2), which can operate around own critical temperature T_c. The n-T1* and n-T2* values are referred to the superconducting elements without the Andreev mirrors.

							$\nu/\delta\nu$		
n-T	T_c (mK)	τ (μs)	τ_{eff} (μs)	NEP_{TFN} (W/$\sqrt{\mathrm{Hz}}$)	NEP_{tot} (W/$\sqrt{\mathrm{Hz}}$)	$\delta\nu$ (GHz)	100 GHz	300 GHz	1 THz
1	128	6	0.01	5.2×10^{-20}	5.2×10^{-20}	100	1	3	10
1*		6	0.01	1.1×10^{-16}	4.7×10^{-16}	2×10^5	4×10^{-4}	1×10^{-3}	4×10^{-3}
2	139	5	0.2	6.7×10^{-20}	6.7×10^{-20}	540	0.18	0.55	1.8
2*		5	0.2	1.5×10^{-16}	8.3×10^{-15}	1×10^6	8×10^{-5}	2×10^{-4}	8×10^{-4}

The thermal fluctuation noise is given by[23]

$$NEP_{TFN} = \sqrt{4k_B \Lambda G_{th,A} T_{c,A}{}^2}, \tag{10}$$

where $\Lambda = n/(2n+1)$ describes the effect of the temperature gradient across the thermal link. Our nano-TESs show an extremely low thermal fluctuation noise, $NEP_{TFN,1} = 5.2 \times 10^{-20}$ W/$\sqrt{\text{Hz}}$ and $NEP_{TFN,2} = 6.7 \times 10^{-20}$ W/$\sqrt{\text{Hz}}$, since G_{th} is limited by the small volume of the active region.

The Johnson noise is originated by the charge transport, when the nano-TES is in the normal state. The related *NEP* is written as[23]

$$NEP_{Jo} = \sqrt{4k_B R_A(T_c) T_{c,A}} \frac{G_{th,A} T_{c,A}}{V\alpha} \sqrt{1 + 4\pi^2 f^2 \tau_{eff}^2}, \tag{11}$$

where $R_A(T_c) \simeq 40\,\Omega$ is the value of R_A at T_c, V is the voltage drop, and f is the signal bandwidth. In order to detect the temperature variations in A, we chose a signal bandwidth $f_1 = 100$ MHz $\geq 1/\tau_{eff,1}$ and $f_2 = 5$ MHz $\geq 1/\tau_{eff,2}$ for n-T1 and n-T2, respectively. For $I_{TES} = 15$ nA, our devices show similar normal state resistances ($R_{A,1} \simeq 70\,\Omega$ and $R_{A,2} \simeq 72\,\Omega$) but different values of the electro-thermal parameter ($\alpha_1 = 2742$ and $\alpha_2 = 122$). Therefore, the Johnson contributions to the noise equivalent power are $NEP_{Jo,1} = 6 \times 10^{-23}$ W/$\sqrt{\text{Hz}}$ and $NEP_{Jo,2} = 2 \times 10^{-21}$ W/$\sqrt{\text{Hz}}$ for n-T1 and n-T2, respectively.

Finally, the shunt noise is related to charge fluctuations through R_{sh}. Its contribution to the *NEP* reads[23]

$$NEP_{sh} = \sqrt{4k_B R_{sh} T_{bath}} \frac{G_{th,A} T_{c,A}}{V\alpha} \times \sqrt{(1-L_0)^2 + 4\pi^2 f^2 \tau_{eff}^2}, \tag{12}$$

where $L_0 = \alpha/n$ is the loop gain. Since the shunting resistor needs to satisfy $R_{sh} \ll R_A$, the contribution of NEP_{sh} is usually negligible compared to Johnson noise. Indeed, in our nano-TESs, we have $NEP_{sh,1} = 3 \times 10^{-24}$ W/$\sqrt{\text{Hz}}$ and $NEP_{sh,2} = 1 \times 10^{-22}$ W/$\sqrt{\text{Hz}}$ for n-T1 and n-T2, respectively.

The total noise equivalent power of our nano-TESs is dominated by the thermal fluctuation contribution, that is, Johnson and shunt resistor noise is negligible, and it shows state-of-the-art values $NEP_{tot,1} = 5.2 \times 10^{-20}$ W/$\sqrt{\text{Hz}}$ and $NEP_{tot,2} = 6.7 \times 10^{-20}$ W/$\sqrt{\text{Hz}}$ for TES technology.[42]

A full analysis of nano-TES performance as a bolometer requires an evaluation of the dynamic range in response to large signals. The saturation power in the limit of voltage bias and the narrow superconducting-to-normal-state transition can be written as[38]

$$P_{sat} = \left(1 - \frac{R_A(T_c)}{R_A}\right) P_{e-ph}, \tag{13}$$

where $R_A(T_c) \simeq 40\,\Omega$ is the resistance of the active region at T_c and $R_A \simeq 70\,\Omega$ is the normal-state resistance. The saturation power ranges approximately from 50 to 100 aW for both devices, thus confirming the predicted high extremely sensitivity of our structures when operated as nano-TESs. These values are promising and well suited in medical, industrial, and astronomical applications. It is anyways possible to increase the saturation power by increasing the heat losses through the phonons, that is, by increasing the active region volume, with the simultaneous increase of the *NEP*.

We now consider devices characterized by the same structure of our nano-TESs, but fabricated without the lateral aluminum banks, namely, they are completely made of the Al/Cu bilayer. The result of this structure is the absence of heat confinement in the small nanowire and the increase of the net device volume to about 1.8×10^{-14} m^3. On the one hand, this change of structure does not affect the thermal response time since both the heat capacity and the thermal conductance depend linearly on the volume [see Eqs. (7) and (8), respectively]. On the other hand, the total noise equivalent power is strongly influenced by the volume increase ($NEP_{tot,1^*} = 5 \times 10^{-16}$ W/$\sqrt{\text{Hz}}$ and $NEP_{tot,2^*} = 8 \times 10^{-15}$ W/$\sqrt{\text{Hz}}$). In particular, NEP_{Jo} and NEP_{sh} depend linearly on G_{th}, thus showing the larger worsening ($NEP_{Jo,1^*} = 4 \times 10^{-16}$ W/$\sqrt{\text{Hz}}$, $NEP_{Jo,2^*} = 5 \times 10^{-16}$ W/$\sqrt{\text{Hz}}$ and $NEP_{sh,1^*} = 4 \times 10^{-16}$ W/$\sqrt{\text{Hz}}$, $NEP_{sh,2^*} = 6 \times 10^{-16}$ W/$\sqrt{\text{Hz}}$) and becoming sizable with respect to thermal fluctuations ($NEP_{TFN,1^*} = 1 \times 10^{-16}$ W/$\sqrt{\text{Hz}}$ and $NEP_{TFN,2^*} = 1.4 \times 10^{-16}$ W/$\sqrt{\text{Hz}}$). Therefore, the removal of AM has a heavy negative impact on the detection performance of the TES bolometer.

B. Calorimeter

In single-photon detection, the value of τ_{eff} determines the minimum speed of the readout electronics necessary to detect a single photon. Moreover, it defines the dead time, that is, the minimum time interval between two incoming photons in order to be recorded as two different events. The NETF ensures that the energy injected into the sensor by the single-photon absorption is efficiently removed by decreasing its Joule overheating instead of being dissipated through the substrate, thus compensating for the initial temperature increase.

The fundamental figure of merit for a single-photon detector is the frequency resolution $\delta\nu$, that is, the minimum photon frequency detected by the sensor. For the nano-TES, it is defined as[12]

$$\delta\nu = \frac{2.36}{h} \sqrt{4\sqrt{\frac{n}{2}} k_B T_c^2 \frac{C_{e,A}}{\alpha}}. \tag{14}$$

Since the minimum detectable single-photon energy depends on α, our nano-TESs show different values of $\delta\nu$. In particular, we have $\delta\nu_1 \simeq 100$ GHz ($\delta E_1 \simeq 0.4$ meV) and $\delta\nu_2 \simeq 540$ GHz ($\delta E_2 \simeq 2$ meV) for n-T1 and n-T2, respectively. Accordingly, the resolving power ($\nu/\delta\nu$), which indicates the sensitivity in detecting radiation of a specific energy, achieves values larger than 1 for $\nu \geq 100$ GHz for n-T1, as shown in Fig. 6. We note that the sensitivity of the devices could be further improved by increasing the sharpness of the superconducting to normal-state transition of the active region, i.e., increasing the value of α.

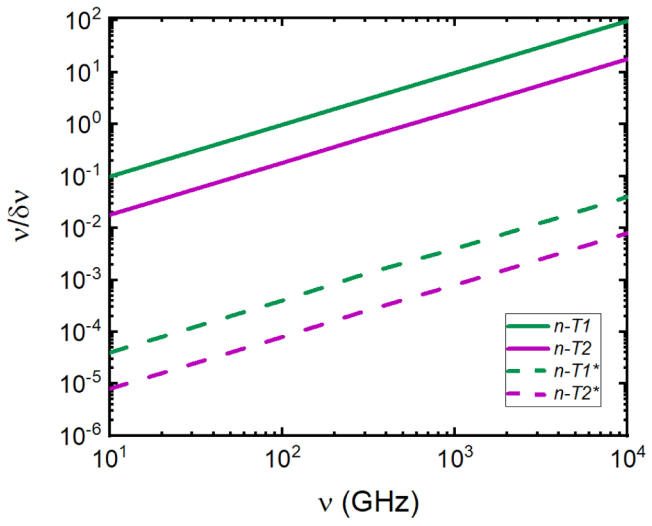

FIG. 6. Resolving power as a function of single-photon frequency for n-T1 (green) and n-T2 (purple). The dashed lines represent similar devices not equipped with the Andreev mirrors. The presence of Andreev mirrors improved the resolving power of more than three orders of magnitude.

In the absence of AM, the electron heat capacitance increases of about seven orders of magnitude due to the volume increase. Therefore, the frequency resolution downgrades of more than three orders of magnitude (see Table I), and the devices could operate only above 300 THz.

VII. MULTIPLEXING CIRCUITS FOR DETECTOR ARRAYS

Astronomy and astrophysical experiments require telescopes equipped with arrays of hundreds or thousands of detectors. Therefore, efficient multiplexing schemes are fundamental to decrease the wiring, lower the related noise, and reduce the mechanical and thermal loads. Several multiplexing architectures differing for the output signals are used: time division multiplexing (TDM), code division multiplexing (CDM), frequency division multiplexing (FDM), and microwave resonator (MR) based readout.[43]

For the frequency operation range and the target applications of our nano-TESs, FDM and MR represent the optimal strategies to create multipixel detectors. Thus, we will estimate the circuit parameters to build arrays of our nano-TESs.

A. Frequency division multiplexing

The FDM circuit is schematically shown in Fig. 7(a).[44–46] Each unit cell operates at its own frequency $[f_n = 1/(2\pi\sqrt{L_nC_n})]$ defined by the RCL circuit and adequately separated from the others to avoid crosstalk. The signal bandwidth of each pixel is larger than the relaxation effective timescale of the nano-TES after the photon absorption $(BW > 1/\tau_{eff})$ suppressing all noise signals outside the band. In order to have a signal bandwidth $[BW = R_A(T_c)/(2\pi L_n)]$ constant for each pixel of the array, the same inductance is usually set for every channel. For example, considering the values of n-T2, we propose a bandwidth BW of 60 kHz, an inductance of 10 μH, and a capacitance range between 10 pF and 25 pF to have ∼31 pixels for an array. Therefore, each pixel has a resonance frequency between 10 MHz and 16 MHz, and it is spaced of 200 kHz to suppress crosstalk. The total signal is measured with a single SQUID amplifier of time constant shorter than the effective pulse recovery time to follow the current variation in the nano-TES ($\tau_s \ll \tau_{eff}$). Its bandwidth BW of 20 MHz is consistent with state-of-the-art

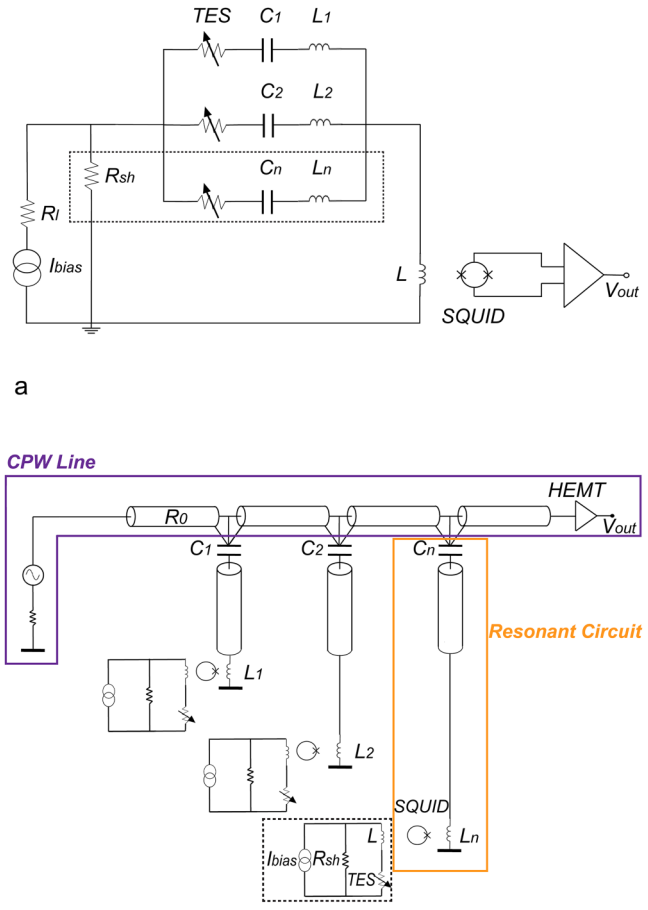

FIG. 7. Multiplexing readout circuits. (a) Scheme of frequency division multiplexing (FDM) readout. FDM is composed by N independent unit cells, which resonate at different frequencies set by the RLC circuit [$L_n = 10\,\mu$H, a capacitance range C between 10 pF and 25 pF, $R_A(T_c) = 40\,\Omega$]. Their frequencies are summed and coupled with a SQUID linked to an amplifier. (b) Scheme of microwave resonator (MR) based multiplexing readout. The schematic circuit is formed by N independent unit cells coupled with an RC resonant circuit, composed by an inductance L, a coaxial cable, and a capacitance C, through a SQUID determining a unique frequency for each resonator. All resonators are read out by a frequency comb applied by an AC generator through a Coplanar Waveguide (CPW) Line. The signal can be amplified by an High Electron Mobility Transistor (HEMT) ($R_0 = 50\,\Omega$, C_n between 60 pF and 2 nF).

SQUID amplifiers.[47,48] Custom LC lithographed boards with multiplexing factors >50 can be fabricated to this end. The generation of tones and subsequent demodulation can be handled by electronic boards equipped with Field Programmable Gate Arrays (FPGAs) suitably designed.[49]

B. Microwave resonator multiplexing

The MR multiplexing exploits a SQUID amplifier connecting the sensing elements of each pixel to a different RLC resonant circuit [see Fig. 7(b)]. This configuration maximizes the dynamic range per pixel and removes the limit on the pixel number, but the system is more bulky. Photon absorption shifts the resonance of the related circuit, which is connected in parallel and excited simultaneously to all the others. Then, the transmitted signals are summed into a low noise amplifier, such as the high electron mobility transistor (HEMT) placed at a higher temperature. The bandwidth of n-T2 is $BW = 5$ MHz. Considering a SQUID amplifier with bandwidth $BW_s = 10$ MHz, we can choose resonant circuits with bandwidth $BW_r = 50$ MHz separated by 50 MHz in the frequency range going from 300 MHz to 2 GHz. To this end, each line could implement systems with a resistance of 50 ~Ω, a fixed inductance of 0.2 μF, and capacitance values between 0.04 pF and 1.4 pF. Therefore, the MR would allow to build arrays of nano-TESs with high dynamic range, low power dissipation, and giving the possibility to select a larger bandwidth.

VIII. SUMMARY AND CONCLUSIONS

We have presented an extra-sensitive and optimized miniaturized structure, which can be used as a nanoscale transition edge sensor (nano-TES). The ultra-low volume of the active region and the exploitation of heat barriers, the so-called Andreev mirrors, ensure the optimal thermal efficiency of the devices. In addition, the engineering of the working temperature, thanks to the superconducting inverse proximity effect, allows full control of the nano-TES performance. To extract all the device parameters and determine the performance in both the bolometer and calorimeter operation, we performed a complete series of experiments. On the one hand, by characterizing electrically the nano-TES, we measured the critical current and the critical temperature of the active region. On the other hand, we fabricated and characterized a secondary device equipped with superconducting tunnel probes extracting the spectral and thermal properties of A.

Starting from the experimental data, we calculated the performance of our device when operated as a nano-TES by employing widespread and well-known equations. The nano-TES is predicted to reach a total noise equivalent power of $\sim 5 \times 10^{-20}$ W/$\sqrt{\text{Hz}}$, limited exclusively by the thermal fluctuations, when operated as a bolometer. In single-photon detection, our device shows the best frequency resolution of ~100 GHz, thus having the potential to operate in the THz and sub-THz regime with a relaxation time of ~10 ns.

With its simple design, the nano-TES could be implemented in widespread multiplexing circuits (FDM and MW resonators) for detector arrays in multipixel gigahertz cameras.[43] As a consequence, the nano-TES could become an asset as a bolometer and a calorimeter for astronomy and astrophysics research, detecting cosmic microwave background[1] and atomic vibration in galaxy cluster[2] and be the key for searching axions,[3,7,8] one of the principal candidates of dark matter. Moreover, it could find application for medical imaging,[25] industrial quality controls,[26] and security[27] in the THz band.

ACKNOWLEDGMENTS

The authors acknowledge A. Tartari and G. Lamanna for fruitful discussions. The authors acknowledge the European Union's Horizon 2020 research and innovation programme under Grant No. 777222 ATTRACT (Project T-CONVERSE) and under Grant Agreement No. 800923-SUPERTED. The authors acknowledge CSN V of INFN under the technology innovation grant SIMP. The work of F.P. was partially supported by the Tuscany Government (Grant No. POR FSE 2014-2020) through the INFN-RT2 172800 project. The work of V.B. is partially funded by the European Union (Grant No. 777222 ATTRACT) through the T-CONVERSE project. G.S. acknowledges the ASI under Grant No. 2016-24-H.0. The authors declare that they have no conflict of interest.

DATA AVAILABILITY

The data that support the findings of this study are available from the corresponding author upon reasonable request.

REFERENCES

[1]G. Sironi, "The frequency spectrum of the cosmic microwave background," New Astron. Rev. **43**, 243–249 (1999).
[2]F. Villaescusa-Navarro, S. Planelles, S. Borgani, M. Viel, E. Rasia, G. Murante, K. Dolag, L. K. Steinborn, V. Biffi, A. M. Beck, and C. Ragone-Figueroa, "Neutral hydrogen in galaxy clusters: Impact of AGN feedback and implications for intensity mapping," Mon. Not. R. Astron. Soc. **456**, 3553–3570 (2016).
[3]I. G. Irastorza and J. Redondo, "New experimental approaches in the search for axion-like particles," Prog. Part. Nucl. Phys. **102**, 89 (2018).
[4]U. Seljak and M. Zaldarriaga, "Signature of gravity waves in the polarization of the microwave background," Phys. Rev. Lett. **78**, 2054 (1997).
[5]M. Kamionkowski and E. D. Kovetz, "The quest for B modes from inflationary gravitational waves," Annu. Rev. Astron. Astroph. **54**, 227–269 (2016).
[6]L. Armus, V. Charmandaris, and B. T. Soifer, "Observations of luminous infrared galaxies with the Spitzer Space Telescope," Nat. Astron. **4**, 467–477 (2020).
[7]A. Ringwald, "Exploring the role of axions and other WISPs in the dark universe," Phys. Dark Univ. **1**, 116–135 (2012).
[8]L. M. Capparelli, G. Cavoto, J. Ferretti, F. Giazotto, A. D. Polosa, and P. Spagnolo, "Axion-like particle searches with sub-THz photons," Phys. Dark Univ. **12**, 37–44 (2016).
[9]M. Arik *et al.*, "New solar axion search using the CERN Axion Solar Telescope with 4He filling," Phys. Rev. D **92**, 021101 (2015).
[10]E. Armengaud *et al.*, "Conceptual design of the International Axion Observatory (IAXO)," JINST **9**, T05002 (2014).
[11]K. D. Irwin, "Seeing with superconductors," Sci. Am. **295**, 86–94 (2006).
[12]K. D. Irwin, "An application of electrothermal feedback for high resolution cryogenic particle detection," Appl. Phys. Lett. **66**, 1998 (1995).
[13]B. S. Karasik and R. Cantor, "Demonstration of high optical sensitivity in far-infrared hot-electron bolometer," Appl. Phys. Lett. **98**, 193503 (2011).
[14]A. Monfardini *et al.*, Proc. SPIE **9914**, 99140N (2016).
[15]P. Khosropanah *et al.*, Proc. SPIE **7741**, 77410L (2010).
[16]P. de Visser, J. Baselmans, J. Bueno *et al.*, "Fluctuations in the electron system of a superconductor exposed to a photon flux," Nat. Commun. **5**, 3130 (2014).
[17]J. Wei, D. Olaya, B. S. Karasik, S. V. Pereverzev, A. V. Sergeev, and M. E. Gershenson, "Ultrasensitive hot-electron nanobolometers for terahertz astrophysics," Nat. Nanotechnol. **3**, 496–500 (2008).

[18]R. Kokkoniemi *et al.*, "Nanobolometer with ultralow noise equivalent power," Commun. Phys. **2**, 124 (2019).
[19]L. S. Kuzmin *et al.*, "Photon-noise-limited cold-electron bolometer based on strong electron self-cooling for high-performance cosmology missions," Commun. Phys. **2**, 104 (2019).
[20]P. Virtanen, A. Ronzani, and F. Giazotto, "Josephson photodetectors via temperature-to-phase conversion," Phys. Rev. Appl. **9**, 054027 (2018).
[21]F. Paolucci, N. Ligato, V. Buccheri, G. Germanese, P. Virtanen, and F. Giazotto, "Hypersensitive tunable Josephson escape sensor for gigahertz astronomy," Phys. Rev. Appl. **14**, 034055 (2020).
[22]D. Alesini *et al.*, "Status of the SIMP project: Toward the single microwave photon detection," J. Low Temp. Phys. **199**, 348–354 (2020).
[23]T. Bergmann, "Energy resolving power of transition edge x-ray microcalorimeters," Ph.D. dissertation (University of Utrecht, 2004).
[24]A. F. Andreev, "The thermal conductivity of the intermediate state in superconductors," Sov. Phy. JETP **19**, 1228–1231 (1964).
[25]Q. Sun, Y. He, K. Liu, S. Fan, E. P. J. Parrott, and E. Pickwell-MacPherson, "Recent advances in terahertz technology for biomedical applications," Quant. Imaging Med. Surg. **7**, 345–355 (2017).
[26]F. Ellrich, M. Bauer, N. Schreiner *et al.*, "Terahertz quality inspection for automotive and aviation industries," J. Infrared Millim. Terahertz Waves **41**, 470–489 (2020).
[27]A. Rogalski and F. Sizov, "Terahertz detectors and focal plane arrays," Opto-Electron. Rev. **19**, 346 (2011).
[28]M. Tinkham, *Introduction to Superconductivity* (McGraw Hill, 1996).
[29]F. Giazotto, T. T. Heikkila, A. Luukanen, A. M. Savin, and J. P. Pekola, "Opportunities for mesoscopics in thermometry and refrigeration: Physics and applications," Rev. Mod. Phys. **78**, 217–274 (2006).
[30]H. Courtois, M. Meschke, J. T. Peltonen, and J. P. Pekola, "Origin of hysteresis in a proximity Josephson junction," Phys. Rev. Lett. **101**, 067002 (2008).
[31]J. F. Cochran and D. E. Mapother, "Superconducting transition in aluminum," Phys. Rev. **111**, 132 (1958).
[32]P. G. De Gennes, "Boundary effects in superconductors," Rev. Mod. Phys. **36**, 225 (1964).
[33]V. G. Kogan, "Coherence length of a normal metal in a proximity system," Phys. Rev. B **26**, 88 (1982).
[34]R. Meservey and P. M. Tedrow, "Properties of very thin aluminum films," J. Appl. Phys. **42**, 51 (1971).
[35]F. C. Wellstood, C. Urbina, and J. Clarke, Phys. Rev. B **49**, 5942 (1994).
[36]R. Bosisio, P. Solinas, A. Braggio, and F. Giazotto, "Photonic heat conduction in Josephson-coupled Bardeen-Cooper-Schrieffer superconductors," Phys. Rev. B **93**, 144512 (2016).
[37]T. T. Heikkilä, M. Hatamib, and G. E. W. Bauerb, "Electron–electron interaction induced spin thermalization in quasi-low-dimensional spin valves," Solid State Commun. **150**, 475 (2010).
[38]K. D. Irwin and G. C. Hilton, *Cryogenic Particle Detection*, Topics in Applied Physics Vol. 99 (Springer, 2005).
[39]K. D. Irwin, "Phonon-mediated particle detection using superconducting tungsten transition-edge sensors," Ph.D. thesis (Stanford University, 1995).
[40]J. C. Mather, "Bolometer noise: Nonequilibrium theory," Appl. Opt. **21**, 1125–1129 (1982).
[41]S. Lee, J. M. Gildemeister, W. Holmes, A. T. Lee, and P. L. Richards, "Voltage-biased superconducting transition-edge bolometer with strong electrothermal feedback operated at 370 mK," Appl. Opt. **37**, 3391–3397 (1998).
[42]K. Morgan, "Hot science with cool sensors," Phys. Today **71**, 28–34 (2018).
[43]J. N. Ullom and D. A. Bennet, "Review of superconducting transition-edge sensors for x-ray and gamma-ray spectroscopy," Supercond. Sci. Technol. **28**, 084003 (2015).
[44]T. M. Lanting, H. Cho, J. Clarke, M. Dobbs, A. T. Lee, P. L. Richards, H. Spieler, and A. Smith, Proc. SPIE **4855**, 172–181 (2003).
[45]A. Tartari, A. M. Baldini, F. Cei, L. Galli, M. Grassi, D. Nicol, M. Piendibene, F. Spinella, D. Vaccaro, and G. Signorelli, "Development and testing of the FDM read-out of the TES arrays aboard the LSPE/SWIPE balloon-borne experiment," J. Low Temp. Phys. **199**, 212–218 (2020).
[46]J. Yoon, J. Clarke, J. M. Gildemeister, A. T. Lee, M. J. Myers, P. L. Richards, and J. T. Skidmore, "Single superconducting quantum interference device multiplexer for arrays of low-temperature sensors," Appl. Phys. Lett. **78**, 371 (2001).
[47]M. Mück, M.-O. Andr, and J. Clarke, "Radio-frequency amplifier based on a niobium dc superconducting quantum interference device with microstrip input coupling," Appl. Phys. Lett. **72**, 2885 (1998).
[48]M. E. Huber *et al.*, "DC SQUID series array amplifiers with 120 MHz bandwidth," IEEE Trans. Appl. Supercond. **1**, 1251–1256 (2001).
[49]A. M. Dobbs *et al.*, "Frequency multiplexed SQUID readout of large bolometer arrays for cosmic microwave background measurements," Rev. Sci. Instrum. **83**, 073113 (2012).